Nanoscale

Accepted Manuscript

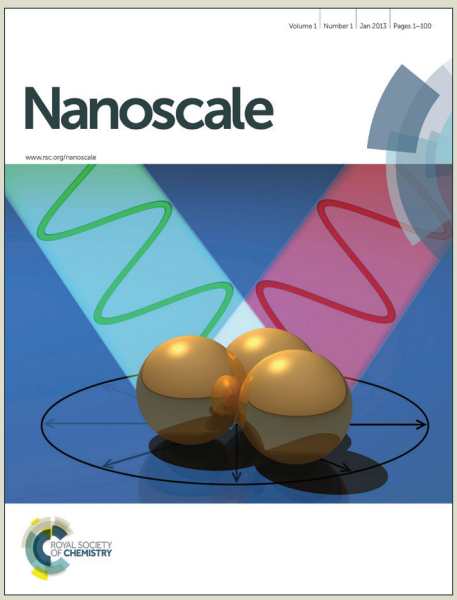

ROYAL SOCIETY OF CHEMISTRY

www.rsc.org/nanoscale

One-pot solvothermal synthesis of graphene wrapped rice-like ferrous carbonate nanoparticles as anode materials for high energy lithium-ion batteries

Fan Zhang [a], Ruihan Zhang [a], Jinkui Feng [a]*, Lijie Ci [a], Shenglin Xiong [b], Jian Yang [b], Yitai Qian [b*], Lifei Li[b*]

[a]*Key Laboratory for Liquid-Solid Structural Evolution & Processing of Materials (Ministry of Education), School of Materials Science and Engineering, Shandong University, Jinan 250061, China*

[b]*School of Chemistry and Chemical Engineering, Shandong University, Jinan 250100, PR China*

**Corresponding author: Jinkui Feng, E-mail: jinkuifeng@sdu.edu.cn*

Abstract:

Well dispersed rice-like $FeCO_3$ nanoparticles were produced and combined with reduced graphene oxide (RGO) via a one-pot solvothermal route. SEM characterizations show that rice-like $FeCO_3$ nanoparticles are homogeneously anchored on the surface of the graphene nanosheets, the addition of RGO is helpful to form a uniform morphology and reduce the particle size of $FeCO_3$ to nano-grade. As anode materials for lithium-ion batteries, the $FeCO_3$/RGO nanocomposites exhibit significantly improved lithium storage properties with a large reversible

capacity of 1345 mAh g^{-1} for the first cycle and capacity retention of 1224 mAh g^{-1} after 50 cycles and with a good rate capability compared with pure $FeCO_3$ particles. The superior electrochemical performance of the $FeCO_3$/RGO nanocomposites electrode compared to the pure $FeCO_3$ electrode can be attributed to the well dispersed RGO which enhances the electronic conductivity and accommodate the volume change during the conversion reactions. Our study shows that $FeCO_3$/RGO nanocomposite could be a suitable candidate for high capacity lithium-ion battery.

Keywords: Reduced graphene oxide; Ferrous carbonate; Anode; Solvothermal; Lithium-ion battery

1. Introduction

Lithium-ion batteries (LIBs) have become one of the most promising energy storage devices because of their high energy density, light weight and low cost [1-4]. Due to the low theoretical capacity and unsatisfactory high-rate performances of commercialized graphite anodes, numerous efforts have been made to develop alternative high-performance anode materials for next generation LIBs. For example, transition-metal based materials have been proved to be potential candidates as anode materials for lithium ion batteries, including various transition-metal oxides (such as Co_3O_4 [5, 6], Fe_3O_4 [7, 8] and MnO_2 [9]) and their oxysalts (such as transition-metal germanates [10-12], oxalates [13, 14] and carbonates [15-26]), because of their high theoretical specific capacity, natural abundance and intrinsic

safety.

As a family of important functional materials, transition metal carbonates have attracted many attentions as they have potential applications in catalyst support, surface engineering, gas adsorption and separation and so on [27-29]. Beyond that, transition metal carbonates have also been verified to be promising anode materials for lithium ion batteries. Aragón et al. first carried out the analysis of electrochemical performance of $MnCO_3$. Its initial reversible capacity was 670 $mAhg^{-1}$ when cycled at the current rate 0.25 C in the voltage range 0-3.0 V [15]. Latter, Ding et al further verified that the $CoCO_3$, $ZnCO_3$, $CuCO_3$ and their composites could also deliver a reversible capacity as high as 800 mAh g^{-1}, enable transition metal carbonates to be novel high capacity anode materials [17-23]. It is worth noting that the observed reversible capacities of transition metal carbonates are always higher than their theoretical capacities calculated from electrochemical reactions and the extra capacity could be ascribed to the capacitive contribution of Faradic and non-Faradic reasons [15-26]. For example, Su discovered that $CoCO_3$ microspheres exhibited a reversible capacity of 930 $mAhg^{-1}$ (40 cycles, at 1C), which was higher than its theoretical value (450 mAh g^{-1}), he verified that not only Co^{2+} but also CO_3^{2-} are involved in the electron transfer, C^{4+} in CO_3^{2-} is reduced to C^0 or other low-valence C under the electrochemical catalysis of newly-generated Co nanoparticles [23]. However, capacity-fading was observed for these transition metal carbonates. Taking $MnCO_3$ as example, a capacity of only 450 mAh g^{-1} was noted after 25 cycles, which is owing to the huge volume change during conversion process and the poor

electrical conductivity of carbonates [15].

As we know, using conductive active materials or adding conductive substrates such as graphene or metals could optimize the electrochemistry performances of anode materials [30-35]. Reduced graphene oxide (RGO) is well known due to its special 2D structure, superior electronic conductivity and large activated surface area. By compositing with RGO, the electrochemical performance of anode materials could be greatly enhanced [33-36]. As reported by Xia, the $CoFe_2O_4$/RGO nanocomposite electrode can deliver a high reversible specific capacity up to 1082 mAh g^{-1} as well as better cycling stability and rate capability compared with that of the pure $CoFe_2O_4$ nanoparticles. The RGO not only helps to relieve the volume change of the active materials but also offers an enhanced electrical contact [35].

Among transition metal carbonates, $FeCO_3$ have many obvious advantages, for example, low cost, abound resource, green character and high theoretical capacity, moreover, it can be invited as the precursor to prepare Fe_3O_4. Assuming that not only Fe^{2+} will reduce to metallic Fe^{0+}, but also C^{4+} in CO_3^{2-} can be reduced to C^0 in the process of electrochemical reaction, pure $FeCO_3$ have a very high theoretical capacity about 1620 mAh g^{-1}, which can be a suitable anode material candidate for high capacity lithium-ion battery [22-24]. Based on these concepts, we have developed a facile one-pot solvothermal method to synthesize the $FeCO_3$/RGO nanocomposite, which consists of rice-like $FeCO_3$ nanoparticles and reduced graphene sheets. According to our observations, RGO is helpful for $FeCO_3$ crystal to form a uniform morphology and reduce the particle size to nano-grade. When used

as the anode material for LIBs, the $FeCO_3$/RGO nanocomposite exhibit a large reversible capacity of 1345 mAh g^{-1} for the first cycle and capacity retention of 1224 mAh g^{-1} after 50 cycles and with a good rate capability, which are all better than pure $FeCO_3$ electrode.

2. Experimental

2.1. Synthesis of graphene oxide, rice-like $FeCO_3$ nanoparticles and $FeCO_3$/RGO nanocomposites.

All the concerned reagents were of analytic grade and used without further purification. The graphene oxide (GO) was synthesized from natural flake graphite power through a modified Hummers method. Rice-like $FeCO_3$ nanoparticles: In a typical procedure, 1.08 g $FeCl_3 \cdot 6H_2O$ was completely dissolved into 50mL distilled water and stirred for 30 min. Next, 24 mL 0.5 M Na_2CO_3 aqueous solution was added dropwise. Then, 1.00 g ascorbic acid was added into the above solution and stirred for 30 min. Finally, the mixture was transferred into a stainless steel autoclave with a Teflon liner of 100 mL capacity and heated in an oven at 160 ℃ for 12 h, followed by cooling to room temperature. $FeCO_3$/RGO nanocomposites: 40 mg graphene oxide was ultrasonicated into 40 mL deionized water to form suspension A. 1.08 g $FeCl_3 \cdot 6H_2O$ was completely dissolved into 40 mL ethylene glycol (EG)-water (1:1 V/V) under continuous magnetic stirring for 30 min to form solution B. Then suspension A and solution B were mixed together uniformly. Next, 1.27 g Na_2CO_3 was added under stirring. Then, 1.00 g ascorbic acid was added into the above

solution and stirred for 30 min. Finally, the mixture was transferred into a 100 mL Teflon-sealed autoclave and heated in an oven at 160 ℃ for 12 h, followed by cooling to room temperature. The obtained precipitations were separated by filtration, and washed with distilled water and ethanol for several times and dried at 50 ℃ for 6 h. The preparation procedure of $FeCO_3$/RGO nanocomposites is illustrated in Figure 1.

2.2. Sample characterization

The crystal structures and chemical compositions of samples were characterized using X-ray diffraction (XRD, Rigaku Dmaxrc diffractometer, V = 50 kV, I = 100 mA) at a scanning rate of 5 degree/min and Raman spectroscopy. The morphologies of the products were examined by SU-70 thermal field emission scanning electron microscopy (FESEM) and JEM-2100 high resolution transmission electron microscopy (HRTEM). The thermogravimetric analysis (TGA) was performed on a Mettler-Toledo TGA/SDTA851e Thermo Analyzer from room temperature to 800 ℃ at a rate of 5 °C min^{-1}. Raman spectra were recorded on a Horiba Jobin-YVON co-focal laser Raman system with He–Ne 632 nm laser as the excitation source.

2.3. Electrochemical test

Electrochemical performance was measured in 2016 coin-type cells. To prepare the working electrode, 70 wt% active material ($FeCO_3$ nanoparticles and $FeCO_3$/RGO nanocomposites), 20 wt% carbon black and 10 wt% carboxy methyl cellulose sodium (CMC) dissolved uniformly in distilled water were mixed to form a slurry. The resulting paste was cast on a Cu foil substrate and dried in a vacuum oven at 90 ℃

for 24 h to form the electrodes. Li foil was used as counter electrode, and Celgard 2400 as separator. The electrolyte was 1 M $LiPF_6$ dissolved in a 1:1:1 mixture of ethylene carbonate, diethyl carbonate and dimethyl carbonate with 5% fluoro-ethyl carbonate (FEC). The cells were assembled in an atmosphere of high-purity argon in a glove box. Galvanostatic discharge-charge measurements of the cells were carried out with voltage range of 0.01−3 V at various rates. Cyclic voltammetry (CV) tests were performed at a scanning rate of 0.1 mV s^{-1} between 0.01 and 3.0 V (vs. Li/Li^+).

3. Results and discussions

Figure 2(a) shows powder XRD patterns of pure $FeCO_3$ and $FeCO_3$/RGO nanocomposites samples, respectively. All the diffraction peaks can be indexed to a rhombohedral $FeCO_3$ crystal (JCPDS no. 12-0531) with $R\bar{3}C$ space group. $FeCO_3$/RGO nanocomposites show almost the same diffraction as $FeCO_3$ since the diffraction from RGO is too weak to be observed, due to nanocrystalline nature of the particles, the peaks show some broadening. There are no other miscellaneous peaks been detected, confirming that the $FeCO_3$ in $FeCO_3$/RGO nanocomposites is also pure phase [37]. Figure 2(b) shows the Raman spectra of the pure $FeCO_3$ microparticles, GO and $FeCO_3$/RGO nanocomposites. Pure $FeCO_3$ shows no obvious feature peaks, while the Raman spectra of the GO and $FeCO_3$/RGO nanocomposites display G bands corresponding to the first-order scattering of the E_{2g} phonon of sp^2 C atoms and D bands which are ascribed to edge planes and disordered structures [38]. Comparing with the Raman spectrum of the GO, it is obvious to see that the Raman peaks of G-

and D-bands in the Raman spectra of the $FeCO_3$/RGO nanocomposites shift to lower frequencies. The D-band shifted from 1365 to 1350 cm^{-1} while the G-band shifted from 1608 to 1592 cm^{-1}, indicating that GO has been reduced to graphene [39, 40]. It has been reported that the intensity ratio of D-band to G-band (I_D/I_G) will increase when GO is reduced to graphene [38]. For our samples, the ratio of I_D/I_G increases from 1.22 of GO to 1.42 of $FeCO_3$/RGO nanocomposites. The reason for this phenomenon might be that most of the oxygen-containing groups are removed during the reduction process, and the conjugated G network would be re-established. However, the size of the re-established G network is smaller than the original one, which results in the increase in the I_D/I_G ratio [45]. Figure. 2(c) shows the TGA curve of the $FeCO_3$/RGO nanocomposites. The weight loss between 200 and 600 ℃ can be attributed to the decomposition of $FeCO_3$ to Fe_2O_3 and the oxidation of carbon, subtracting the contribution from the theoretical weight loss of $FeCO_3$, the graphene weight ratio in the composites was estimated to 16.1%.

The morphologies of products were characterized by FE-SEM and HRTEM as shown in Figure 3. It can be seen from Figure 3(a) that $FeCO_3$ microparticles with irregular shape and severe aggregation were produced after the solvothermal treatment, the size of $FeCO_3$ microparticles are in the range of 150-250 nm. When RGO was introduced in $FeCO_3$ (Figure 3(b)), most of rice-like $FeCO_3$ nanoparticles with typical diameters of 50 nm and length in the range of 80-120 nm are uniformly dispersed on the graphene nanosheets with almost no aggregation. The high magnification FE-SEM images (Figure 3(c) and 3(d)) clearly show the details of the

morphology of $FeCO_3$/RGO nanocomposites. The almost transparent two-dimensional graphene nanosheets act as supporting substrates for homogeneously anchoring of $FeCO_3$ nanoparticles, building a $FeCO_3$-RGO heteroarchitecture. It is speculated that the addition of RGO could lead to uniform distribution of $FeCO_3$ nanoparticles on the graphene nanosheets and suppress the aggregation of $FeCO_3$ nanoparticles [35, 41]. Figure 3(e) shows the HR-TEM image of $FeCO_3$/RGO nanocomposites and the corresponding SAED pattern, which taken from an individual nanoparticles, indicating that these rice-like $FeCO_3$ nanoparticles are monocrystalline. As obviously observed in the representative HRTEM image (Figure 3(f)), the (006) lattice spacing (0.254 nm) verified the rhombohedral $FeCO_3$ crystal texture.

The electrochemical performances of pure $FeCO_3$ microparticles and $FeCO_3$/RGO nanocomposites were characterized by static-current charge–discharge. The voltage profiles of the 1^{st}, 2^{th}, 10^{th}, 20^{th} and 50^{th} cycles for the pure $FeCO_3$ microparticles and $FeCO_3$/RGO nanocomposite electrodes cycled between 0.01 and 3 V at a current density of 100 mA g^{-1} are shown in Figure 4(a) and 4(b). For pure $FeCO_3$ electrode (Figure 4(a)), during the initial cycle within a range of 0.01-3 V, high specific discharge and charge capacity of 1820 mAh g^{-1} and 1310 mAh g^{-1} can be achieved. The irreversible capacity results from the well-known formation of solid electrolyte interface (SEI) film and other irreversible reactions. The main plateau of SEI is above 0.5 V. The declining plateau from 0.45 V in the first discharge curve is attributed to the conversion reduction of Fe^{2+} to metallic Fe^{0+} accompanied by the reduction of C^{4+} to C^{0+} then to Li_2C_2 [23-25]. During the following de-lithiation

process the cell voltage shows a sloppy signature centered at about 1.7 V vs. Li. The above mentioned reduction plateau vanished upon lithiation to disappear, illustrating a different reaction mechanism. The reversible capacity remains only 680 mAh g^{-1} after 50 cycles. As a comparison, for $FeCO_3$/RGO, there was not such plateau form 0.45 V but a slope form about 1.3 V, which is ascribed to the lithiation process of RGO accompanied with the formation of SEI film [7]. The plateau of $FeCO_3$/RGO is not obvious compared with pure $FeCO_3$. The reason of this phenomenon should be due to the high electronic conductivity of $FeCO_3$/RGO nanocomposites, which facile the phase transformation during the lithaition/de-lithiation progress [7-9]. The capacity retention of $FeCO_3$/RGO (Figure 4(b)) is as high as 1210 mAh g^{-1} after 50 cycles. The high reversible capacity is from the conversion mechanism of Fe^{2+} to Fe and C^{4+} to Li_2C_2 [23-25]. From the cycling result we can see that there is a increase for the capacity at about 30 cycles, which are well recognized to be an electrode activation process [7, 8].

Figure 4(e) compares the cycle and rate performances of the pure $FeCO_3$ microparticles and $FeCO_3$/RGO nanocomposites. For cycle performances, both electrodes are cycled between 0.01 and 3 V at different current density for 100 cycles. It can be seen that the $FeCO_3$/RGO nanocomposites electrode exhibits much better cycling stability than that of the pure $FeCO_3$ electrode. The capacity remains 1224 mAh g^{-1} for the 50 cycles and 1250 mAh g^{-1} for the 100 cycles, which corresponding to 91.0% and 93.2% capacity retention, the obtained reversible capacity of the $FeCO_3$/RGO nanocomposites electrode is much higher than the theoretical capacity of

commercially used graphite anode (372 mAh g^{-1}). As shown in Figure 4(c) and 4(d), the pure graphene electrode can deliver a reversible capacity of about 415 mAh g^{-1} for the first cycle and 352 mAh g^{-1} after 100 cycles. Therefore, the graphene content in the nanocomposite should be controlled in a certain range, otherwise a considerable high graphene content could sacrifice the high specific reversible capacity [35]. For our experiment, subtracting the contribution from the RGO in $FeCO_3$/RGO nanocomposites, a reversible capacity about 1479 mA h g^{-1} can be attributed to the 84.9 wt% $FeCO_3$ after 100 cycles, which is basically close to the theoretical capacities of pure $FeCO_3$ (1620 mAh g^{-1}). It is worth noting that the discharge capacity of $FeCO_3$/RGO nanocomposites electrode appeared to increase slightly after 25 cycles, such an interesting phenomenon is commonly observed for many metal oxides and their oxysalts, which can be attributed to the activation process for the electrochemical reaction of lithium, along with the formation of the polymeric/gel-like film [42-44]. In comparison, the capacity decay for the pure $FeCO_3$ electrode is much serious, only 70.8% (765 mAh g^{-1}) and 62.7% (698 mAh g^{-1}) capacity is remained. Such a significant capacity fading for the pure $FeCO_3$ electrode may be due to its poor electronic conductivity and trends to collapse along with repeated electrochemical reaction processes. In addition, the obtained pure $FeCO_3$ were microparticles with large sizes, which seriously restricted their potentials for lithium storage. In addition to the better capacity retentions, the $FeCO_3$/RGO nanocomposites electrode also exhibit superior rate capacities as shown in Figure 4(c). With increase in current density, the $FeCO_3$/RGO electrode can deliver a reversible capacity of 1224, 1132,

1045 and 974 mAh g^{-1} at a current density of 0.1, 0.5, 1.0 and 1.5 A g^{-1}, respectively. A reversible capacity of 1250 mAh g^{-1} can be achieved after the rate returns to 0.1 A g^{-1}. In contrast, the capacities of pure $FeCO_3$ microparticles prepared under the same condition were only 765, 610, 423 and 314 mAh g^{-1}, respectively. A reversible capacity of 698 mAh g^{-1} can be achieved after the rate returns to 0.1 A g^{-1}. Hence, the result demonstrates that the structure of the nanocomposite is very stable, and the Li^+ ions insertion/extraction process is quite reversible even at the high current rates. It is believed that the addition of RGO could not only suppress the aggregation of $FeCO_3$ nanoparticles but also prevents the restacking of graphene nanosheets, resulting in a large electrode/electrolyte interface area, which facilitate fast lithium ion and electron transport, and RGO can served as an inactive confining buffer to accommodate the volume change during electric cycling, all of these lead to a better electrochemical performance of $FeCO_3$/RGO nanocomposites electrode.

In order to gain better understanding of why $FeCO_3$/RGO nanocomposites exhibit such a superior electrochemical performance compared to pure $FeCO_3$ electrode, EIS measurements were performed as shown in Figure 4(f). The high frequency semicircle corresponds to the charge-transfer resistance Rct and CPE of electrode/electrolyte interface, and the inclined line at about 45-50° angle to the real axis corresponds to the lithium-diffusion process. It shows that the Rct of $FeCO_3$/RGO electrode is 210 Ω, which is significantly lower than that of pure $FeCO_3$ electrode (Rct = 430 Ω). It is believed that the high electrical conductivity of the graphene nanosheets could be maintained in the nanocomposite sample and holds the

$FeCO_3$ nanoparticle tightly in the pores. This action prevents the $FeCO_3$ nanoparticle from aggregation and thereby enlarges the contact area between electrode and electrolyte, resulting in the significant improvement in the kinetic performance of electrochemical lithium insertion/extraction. Therefore, the $FeCO_3$/RGO nanocomposites electrode exhibits considerably enhanced capacity with excellent cycle stability and rate capability.

Cyclic voltammograms were further conducted to investigate the electrochemical behaviors of $FeCO_3$/RGO nanocomposites (Figure 5). Initial cathodic scan reveals two main peaks from 1.3 V, 0.9 V and 0.3 V, in agreement with the initial discharge curve. The first small peak is attributed to Fe^{2+} to Fe^0 and the formation of SEI film, which coincides with many iron oxides. The peak at 0.1 V are the combination of complete reduction of Fe^{2+} to Fe^0 and the CO_3^{2-} decomposition [22-25]. For the anodic scan, the humplike peaks at 1.2 and 1.52 V, and the succeeding broad anodic peaks centered at 1.65 V, are due to the further oxidation of metallic Fe^0 to Fe^{3+}, companied with the re-oxidation of low valence C. The reduction peaks at 0.38 V are replaced by two broad split peaks shifting to 0.92 V with decreased intensity while the peak at 0.1 V remains in the second cycle, indicating partly irreversible processes in the first cycle. Interestingly, the reduction peaks are replaced by a broad split peak shifting to 0.76 V with decreased intensity in the third cycle, which is ascribed to the amorphous nature/crystal structure destruction of the material, reported previously on some metal oxysalts and metal oxides [23-25]. Moreover, the subsequent CV curves overlap well, revealing good reversibility of Li storage performances.

The mechanical stability of the $FeCO_3$/RGO composite was further investigated by Ex-situ SEM imaging for electrodes that were removed from a cell after 100 charge/discharge cycles. Cracks and aggregations on the surface of the pure $FeCO_3$ electrode are observed in Figure 6(a) and (b), which will cause the disconnection of the active materials with the current collector and result in capacity fading. However, No disassembly or cracking of the $FeCO_3$/RGO composite was found (Figure 6(c) and (d)), shows that the $FeCO_3$ was still uniformly anchored on the electrode after cycling.

The greatly enhanced electrochemical performance of the $FeCO_3$/RGO electrode is comparable to bare $FeCO_3$ electrode may be due to the following factors: 1) the graphene coating on the $FeCO_3$ provides a robust elastic buffer to accommodate the large volume change thus maintaining the integrity of individual $FeCO_3$ particles. 2) The RGO network provides a block effect for the aggregation of $FeCO_3$ particles, yielding a higher mechanical strength to better withstand the stress buildup in the electrode; 3) The RGO greatly improved the electronic conductivity and catalyst the conversion reaction of $FeCO_3$, which is proved by Wang's group [34].

4. Conclusions

A facile solvothermal method has been developed to synthesis $FeCO_3$ microparticles and $FeCO_3$/RGO nanocomposites. When evaluated as anode material for lithium-ion batteries, the nanocomposites exhibit high reversible capacity, good cycle performance and good rate capability. The superior electrochemical performance of the nanocomposites electrode is due to the high electronic

conductivity and the high specific area of RGO, which are able to buffer large volume change and enable fast ion and electron transport. These $FeCO_3$/RGO nanocomposites could be used as a promising electrode material for lithium-ion batteries.

Reference

[1] J. M. Tarascon and M. Armand, *Nature*, 2001, **414**, 359-367.

[2] W. H. Li, Z. Z. Yang, J. X. Cheng, X. W. Zhong, L. Gu and Y. Yu, *Nanoscale*, 2014, **6**, 4532–4537.

[3] M.G. Kim and J.Cho, *Adv. Funct. Mater.,* 2009, **19**, 1497-1514.

[4] A. S. Arico, P. Bruce, B. Scrosati, J. M. Tarascon and W. Van Schalkwijk, *Nat. Mater.*, 2005, **4**, 366-372.

[5] J. Liu, H. Xia, L. Lu and D. F. Xue, *J. Mater. Chem.*, 2010, **20**, 1506-1510.

[6] G. L. Xu, J. T. Li, L. Huang, W. Lin and S. G. Sun, *Nano Energy*, 2013, **2** , 394-402.

[7] H. Xia, Y. H. Wan, G. L. Yuan, Y. S. Fu and X. Wang, *J. Power. Sources*, 2013, **241**, 486-493.

[8] J. S. Xu and Y. J. Zhu, *ACS Appl. Mater. Interfaces*, 2012, **4**, 4752-4757.

[9] H. Xia, M. O. Lai and L. Lu, *J. Mater. Chem.,* 2010, **20**, 6896-6902.

[10] J. K. Feng, M. O. Lai and L. Lu, *Electrochem. Commun.,* 2011, **13**, 287-289.

[11] R. Yi, J. K. Feng, D. P. Lv, M. L. Gordin, S. R. Chen, D. W. Choi and D. H. Wang, *Nano Energy,* 2013, **2**, 498-504.

[12] W. Li, Y. X. Yin, S. Xin, W. G. Song and Y. G. Guo, *Energy. Environ. Sci.,* 2012, **7**, 8007-8013.

[13] M. J. Aragón, B. León, C. P. Vicente, J. L. Tirado, A. V. Chadwick, A. Berko and S.-Y. Beh, *Chem. Mater.,* 2009, **21**, 1834-1840.

[14] W. A. Ang, N. Gupta, R. Prasanth and S. Madhavi, *ACS Appl. Mater. Interfaces,*

2012, **4**, 7011-7019.

[15] M. J. Aragón, C. V. Pérez and J. L. Tirado, *Electrochem. Commun.,* 2007, **9**, 1744-1748.

[16] F. Zhang, R. H. Zhang, G. M. Liang, J. K. Feng, L. Lu and Y. T. Qian, *Mater. Lett.*, 2013, **111**, 165-168.

[17] B. Xu, L. Shi, X. W. Guo, L. Peng, Z. X. Wang, S. Chen, G. P. Cao, F. Wu and Y. S. Yang, *Electrochim. Acta,* 2011, **56**, 6464-6468.

[18] M. J. Aragón, B. León, C. P. Vicente and J. L. Tirado, *J. Power. Sources*, 2011, **196**, 2863-2868.

[19] S. Mirhashemihaghighi, B. Leon, C. Perez Vicente, J.L. Tirado, R. Stoyanova, M. Yoncheva, E. Zhecheva, R. Saez Puche, E.M. Arroyo and J.Romero de Paz, *Inorganic Chemistry*, 2012, **51**, 5554-5561.

[20] F. Zhang, R. H. Zhang, J. K. Feng and Y. T. Qian, *Mater. Lett.*, 2014, **114**, 115-118.

[21] Y. Sharma, N. Sharma, G. V. Subba Rao and B. V. R. Chowdari, *J. Mater. Chem.,* 2009, **19**, 5047-5054.

[22] Z. J. Ding, B. Yao, J. K. Feng and J. X. Zhang, *J. Mater. Chem.,* 2013, **1**, 11200-11209.

[23] L. W. Su, Z. Zhou, X. Bin, Q. W. Tang, D. H. Wu and P. W. Shen, *Nano Energy*, 2013, **2**, 276-282.

[24] S. Q. Zhao, Y. Yu, S. S. Wei, Y. X. Wang, C. H. Zhao, R. Liu and Q. Shen, *J. Power. Sources*, 2014, **253**, 251-255.

[25] Y. R. Zhong, L. W. Su, M. Yang, J. P. Wei and Z. Zhou, *ACS Appl. Mater. Interfaces,* 2013, **5**, 11212-11217.

[26] T. Brezesinski, J. Wang, J. Polleux, B. Dunn and S. H. Tolbert, *J. Am. Chem. Soc*, 2009, **131**, 1802-1808.

[27] J. W. Morse, R. S. Arvidson and A. Lüttge, *Chem. Rev.*, 2007, **107**, 342-381.

[28] B. Xu, L. Peng, G. Q. Wang, G. P. Cao and F. Wu, *Carbon,* 2010, **48**, 2361-2380.

[29] Q. C. Zhuang, J. Li and L. L. Tian, *J. Power. Sources,* 2013, **222**, 177-183.

[30] S. M. Paek, E. Yoo and I. Honma, *Nano. Lett.,* 2009, **1**, 72-75.

[31] X. C. Li, X. Y. Xu, F. L. Xia, L. X. Bu, H. X. Qiu, M. X. Chen, L. Zhang and J. P. Gao, *Electrochim. Acta*, 2014, **130**, 305-311.

[32] Y. Sharma, N. Sharma, R. G. V. Subba and B. V. R. Chowdari, *Adv. Funct. Mater.,* 2007, **17**, 2855-2862.

[33] Z. Chen, Y. Yan, S. Xin, W. Li, J. Qu, Y. G Guo and W, G. Song, *J. Mater. Chem. A*, 2013, **1**, 11404-11409.

[34] D. P. Lv, M. L. Gordin, R. Yi, T. Xu, J. X. Song, Y. B. Jiang, D. W. Choi and D. H. Wang, *Adv. Funct. Mater.*, 2014, **24**, 1059-1066.

[35] H. Xia, D. D. Zhu, Y. S. Fu and X. Wang, *Electrochim. Acta*, 2012, **83**, 166-174.

[36] S. X. Jin and C. X. Wang, *Nano Energy*, 2014, **7**, 63-73.

[37] K. H. Seng, M. H. Park, Z. P. Guo, H. K. Liu and J.Cho, *Nano Lett.*, 2013, **13**, 1230-1236.

[38] P. C. Lian, X. F. Zhu, S. Z. Liang, Z. Li, W. S. Yang and H. H. Wang,

Electrochimica Acta, 2010, **55**, 3909-3916.

[39] S. Stankovich, D. A. Dikin, R. D. Piner, K. A. Kohlhaas, A. Kleinhammes, Y. Jia, Y. Wu, S. T. Nguyen and R. S. Ruoff, *Carbon*, 2007, **45**, 1558-1564.

[40] T. N. Lambert, C. A. Chavez, B. Hernandez-Sanchez, P. Lu, N. S. Bell, A. Ambrosini, F. Friedman, T. J. Boyle, D. R. Wheeler and D. L. Huber, *J. Phys. Chem. C*, 2009, **113**, 19812-19818.

[41] J. Qiu, P. Zhang, M. Ling, S. Li, P. Liu, H. Zhao and S. Zhang, *ACS. Appl. Mater. Interfaces,* 2012, **7**, 3636-3642.

[42] W. Li, Y. X. Yin, S. Xin, W. G. Song and Y. G. Guo, *Energy. Environ. Sci.*, 2012, **7**, 8007-8013.

[43] F. Zhang, R. H. Zhang, G. M. Liang, J. K. Feng, L. Lu and Y. T Qian, *Mater. Lett.*, 2013, **111**, 165-168.

[44] J. Liu, H. Xia, L. Lu and D. F. Xue, *J. Mater. Chem.,* 2010, **20**, 1506-1510.

[45] J. Shen, M. Shi, B. Yan, H. Ma, N. Li, M. Ye, *J. Mater. Chem.,* 2011, **21**, 7795-7801.

Figure captions:

Figure 1. Schematic drawing of the preparation process of $FeCO_3$/RGO nanocomposite.

Figure 2. (a) XRD patterns of the as-synthesized $FeCO_3$ microparticles and $FeCO_3$/RGO nanocomposites. (b) Raman spectroscopy of the pure $FeCO_3$ microparticles, GO and $FeCO_3$/RGO nanocomposites. (c) TGA curve of $FeCO_3$/RGO nanocomposites.

Figure 3. FE-SEM images of the pure $FeCO_3$ microparticles and $FeCO_3$/RGO nanocomposites with low magnification (a and b) respectively. FE-SEM images of $FeCO_3$/RGO nanocomposites with high magnification (c and d). HR-TEM image of $FeCO_3$/RGO nanocomposites (e and f) and the corresponding SAED pattern (inset picture of (e)).

Figure 4. Discharge/charge voltage profiles of (a) pure $FeCO_3$ microparticles, (b) $FeCO_3$/RGO nanocomposites and (c) pure graphene electrodes. Cycling performance of (b) pure graphene electrode and (e) pure $FeCO_3$ microparticles and $FeCO_3$/RGO nanocomposites at constant current rate of 0.1 C and the comparison of rate capabilities at various current rates between 0.1 C to 1.5 C. (f) Nyquist plots of pure $FeCO_3$ microparticles and $FeCO_3$/RGO nanocomposites electrodes.

Figure 5. Cyclic voltammograms of $FeCO_3$/RGO nanocomposites electrodes.

Figure 6. Ex-situ FE-SEM images of cycled electrodes (a and b) pure $FeCO_3$ microparticles and (c and d) $FeCO_3$/RGO nanocomposites.

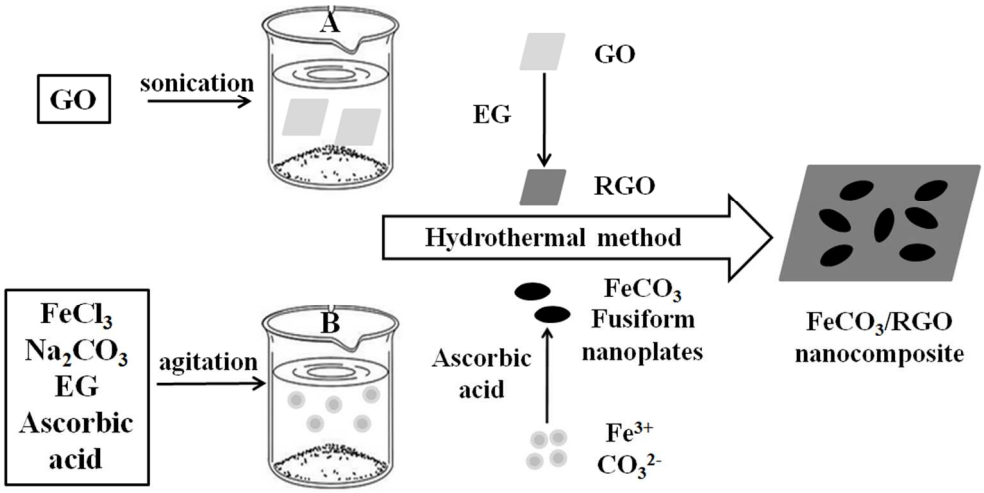

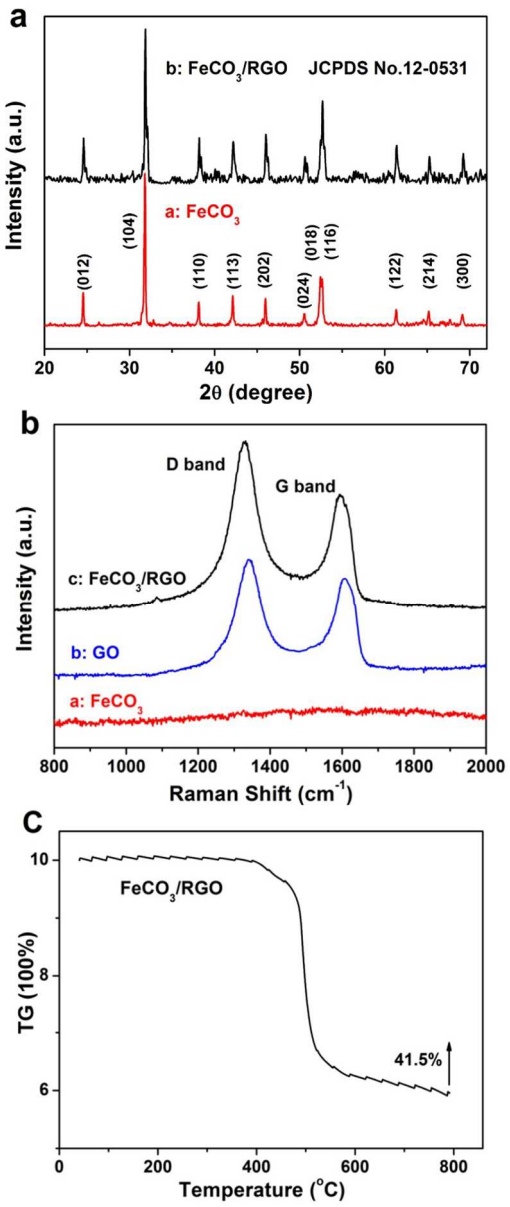

221x519mm (96 x 96 DPI)

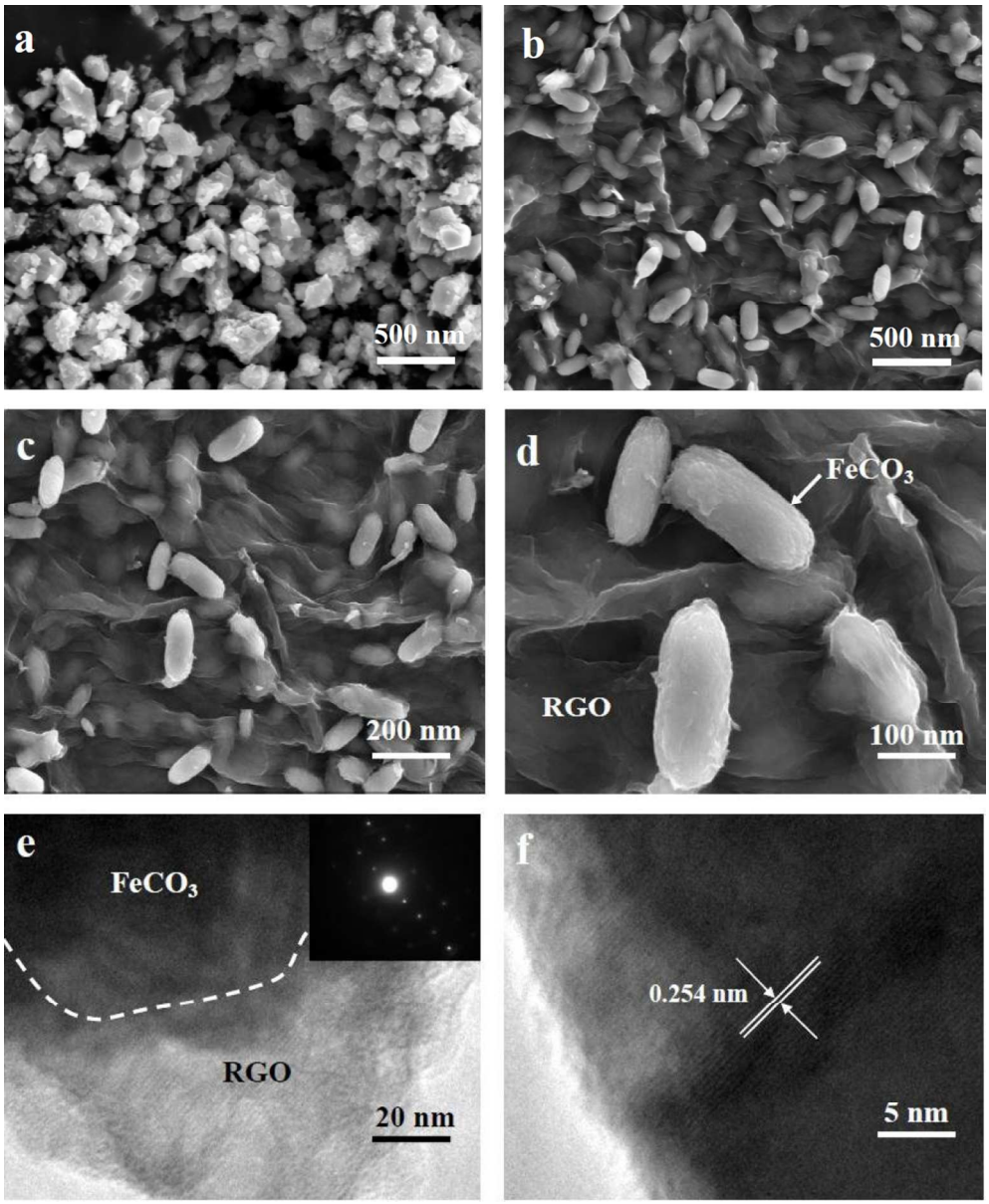

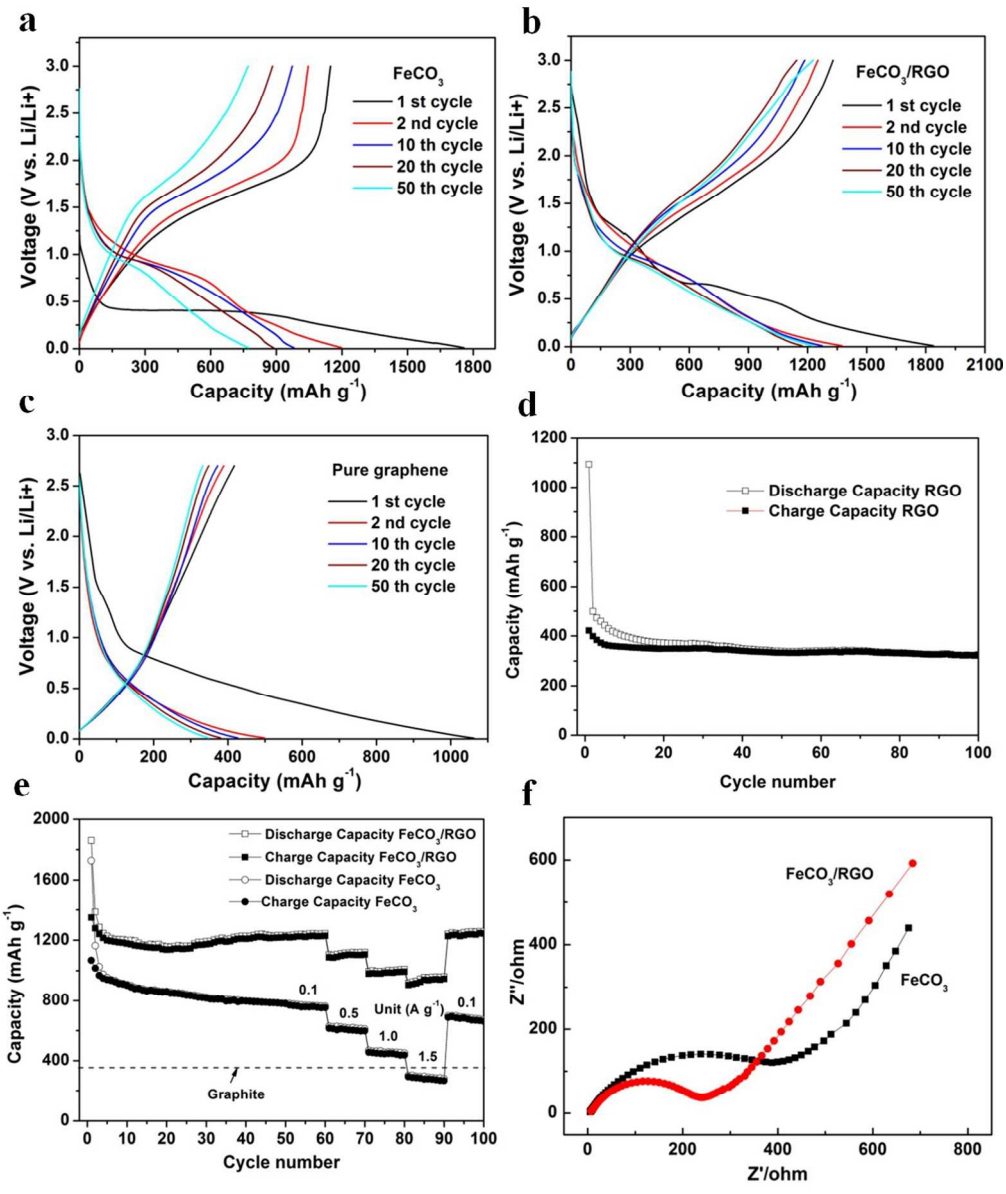

352x421mm (96 x 96 DPI)

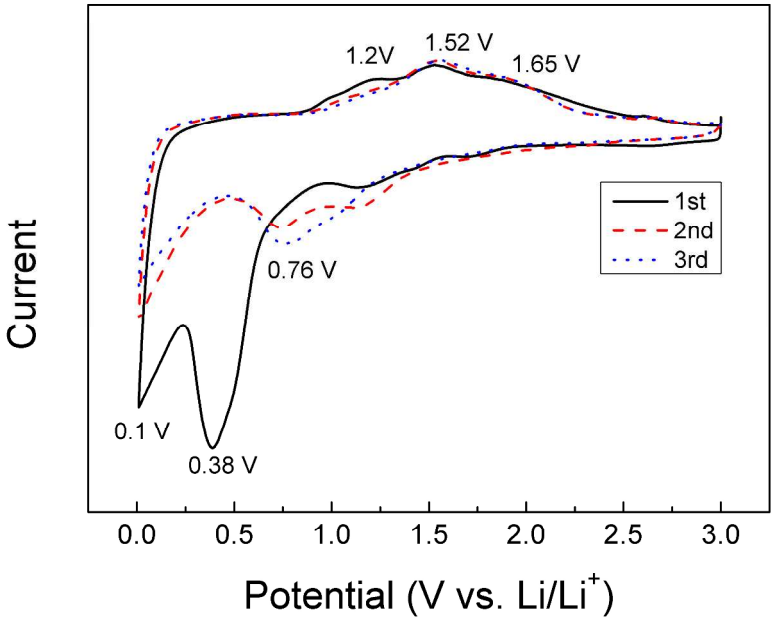

296x209mm (300 x 300 DPI)